




Optimizing Neural Network Surrogate Models: Application to Black Hole Merger Remnants

Lucy M. Thomas ^{1,2,*}, Katerina Chatziioannou ^{1,2,†}, Vijay Varma,³ and Scott E. Field ³

¹*TAPIR, California Institute of Technology, Pasadena, CA 91125, USA*

²*LIGO Laboratory, California Institute of Technology, Pasadena, California 91125, USA*

³*Department of Mathematics, Center for Scientific Computing and Data Science Research, University of Massachusetts, Dartmouth, MA 02747, USA*

(Dated: May 21, 2025)

Surrogate models of numerical relativity simulations of merging black holes provide the most accurate tools for gravitational-wave data analysis. Neural network-based surrogates promise evaluation speedups, but their accuracy relies on (often obscure) tuning of settings such as the network architecture, hyperparameters, and the size of the training dataset. We propose a systematic optimization strategy that formalizes setting choices and motivates the amount of training data required. We apply this strategy on `NRSur7dq4Remnant`, an existing surrogate model for the properties of the remnant of generically precessing binary black hole mergers and construct a neural network version, which we label `NRSur7dq4Remnant_NN`. The systematic optimization strategy results in a new surrogate model with comparable accuracy, and provides insights into the meaning and role of the various network settings and hyperparameters as well as the structure of the physical process. Moreover, `NRSur7dq4Remnant_NN` results in evaluation speedups of up to 8 times on a single CPU and a further improvement of 2,000 times when evaluated in batches on a GPU. To determine the training set size, we propose an iterative enrichment strategy that efficiently samples the parameter space using much smaller training sets than naive sampling. `NRSur7dq4Remnant_NN` requires $\mathcal{O}(10^4)$ training data, so neural network-based surrogates are ideal for speeding-up models that support such large training datasets, but at the moment cannot directly be applied to numerical relativity catalogs that are $\mathcal{O}(10^3)$ in size. The optimization strategy is available through the `gwbonsai` package.

I. INTRODUCTION

Binary black hole (BBH) mergers account for most gravitational waves detected so far [1–12] by the LIGO [13], Virgo [14] and KAGRA [15] detectors. Measuring and interpreting the system properties relies on models for the observed signal [16–18]. Numerical relativity (NR) simulations of the binary dynamics and gravitational emission in full General Relativity provide the only accurate description of the BBH merger, including the late inspiral and merger signals as well as the remnant properties. However, the high computational cost and relatively sparse parameter space coverage [19–21] makes it infeasible to rely solely on NR simulations, as data analysis requires millions of model evaluations. Approximate semi-analytical models for waveforms [22–33] and remnant properties [34–53] that combine analytical insights with fits to NR have therefore been developed.

An alternative approach involves direct surrogate models to the NR simulations, which are fast and accurate approximations to a more computationally intensive underlying model [54]. NR surrogates match simulations more accurately than semi-analytical models, but they are limited by the parameter space coverage and availability of NR catalogs. Existing NR and NR-hybrid surrogate models target both waveforms and remnant properties [55–63]. Surrogate construction option-

ally first reduces the training data to sufficiently sparse, smoothly-varying components, and then fits these components across the parameter space [54]. Fitting methods include polynomials [54, 56], splines [64, 65], Gaussian Process Regression (GPR) [57, 59], or more recently neural networks [66–76].

Neural networks can yield comparable accuracy to other methods while significantly reducing model evaluation time. However, their efficacy hinges on many seemingly arbitrary choices of settings, such as the neural network architecture or its numerous hyperparameters, which are not straightforwardly physically motivated. The impact of these choices is typically not clear until after the expensive training process has been completed and the network’s accuracy can be assessed. The high cost of full network training makes exploring multiple choices for the architecture and hyperparameters cumbersome.

Hyperparameter optimization focuses on finding the best hyperparameters, often within a high-dimensional space, to maximize model performance. Common techniques include grid and random search (simple but often inefficient), Bayesian optimization (uses probabilistic models to balance exploration and exploitation of the search space), and evolutionary algorithms (mimic natural selection through meta-heuristic strategies). Many of these methods are implemented in flexible hyperparameter optimization tools such as Optuna, Ray Tune, Keras Tuner, Auto-sklearn, DEAP, and HyperOpt, making them suitable for a wide range of problems.

Solving the hyperparameter optimization problem

* lmthomas@caltech.edu

† kchatziioannou@caltech.edu

is increasingly important in gravitational wave astrophysics. Gradient-free genetic algorithms, for instance, have been shown to refine deep matched filtering architectures for greater accuracy and compactness [77]. In waveform modeling studies using neural networks [66–76], most hyperparameters are set heuristically or through basic random/grid search. Notable exceptions include neural-network-based waveform models for aligned-spin systems [73, 76] and precessing systems approximated as an aligned-spin system in the coprecessing frame [70]. To date, no work has systematically explored hyperparameter or training-set optimization for fully generic precessing BBH systems.

In this work, we propose a framework that systematically optimizes the training settings, including the network architecture, network hyperparameters, and the amount of training data. As an application of this framework, we consider the remnant surrogate `NRSur7dq4Remnant` [59] which calculates the merger remnant properties (final black hole (BH) mass, spin, and recoil velocity) from the BBH properties (initial BH mass ratio and spins). The remnant mass and spin determine the ringdown mode content [78–83], while the recoil velocity determines whether the remnant is ejected from its host environment [34, 84–88]. For maximum flexibility, we do not work directly with NR data but instead use `NRSur7dq4Remnant` to make training data that we then fit with a neural network.

We address three key elements of efficient and accurate neural network-based surrogates.

1. We explore the interplay between neural network architecture and hyperparameters values toward optimal accuracy. Using optimization techniques, we study the role of various settings, in the process clarifying their role during network training.
2. We examine whether splitting the output parameters among multiple networks allows for specialization in training and improved accuracy without overfitting. We find no accuracy gain from considering parameter subsets separately. What is more, the full 7-dimensional network achieves high accuracy with relatively less aggressive settings than some subset networks.
3. We investigate the relation between the size of the training data and model accuracy, determining the minimum amount of data necessary to achieve high-precision predictions without unnecessary computational overhead. We find that $\mathcal{O}(10^4)$ training data points are required, compared to the $\mathcal{O}(10^3)$ NR points `NRSur7dq4Remnant` was fit on initially.

Using the optimal settings, we train a new neural network-based surrogate model, `NRSur7dq4Remnant_NN`. The accuracy of the new model compared to the underlying model it was trained on is comparable or better than the underlying model’s accuracy to its underlying NR data. The upper 95th percentile error over all 7

output parameters between `NRSur7dq4Remnant_NN` and `NRSur7dq4Remnant` is 1.1×10^{-2} while the same quantity between `NRSur7dq4Remnant` and the original NR data is 4.1×10^{-2} . Moreover, `NRSur7dq4Remnant_NN` unlocks significant computational improvements. When evaluated on a CPU, we obtain speedups of up to 8 times (comparing the median time across the fastest implementation of each model), while batch evaluation on a GPU results in a further speedup of 2,000. The optimization framework is model-agnostic, it is therefore applicable to other surrogates which use interpolation, including waveform surrogates.

We release the optimization code as `gwbonsai` [89]. The package uses optimization procedures from `Optuna` [90] (or alternatively `Hyperopt` [91]), and allows users to automatically optimize network settings as part of the surrogate model construction. It can utilize either a `Tensorflow`[92] or `PyTorch` [93] backend for network training, and produces both GPU-evaluable results designed for batch evaluation and a `NumPy` [94] (or `JAX` [95]) implementation suited for evaluation on CPUs.

The paper is organized as follows. In Sec. II we provide an overview of the construction and training of `NRSur7dq4Remnant_NN`. In Sec. III we develop infrastructure to optimize the neural network architecture and hyperparameters for several subsets of output parameters. In Sec. IV we assess the optimal training dataset size and configuration, again considering several output subsets. In Sec. V we train the final optimized network and evaluate its performance in terms of accuracy, timing, and extrapolation performance, before concluding in Sec. VI. Throughout this paper we use geometric units, $G = c = 1$, unless stated otherwise.

II. MODEL STRUCTURE AND DATASETS

We apply the network optimization framework to the remnant surrogate model `NRSur7dq4Remnant`, and construct a neural network-based surrogate-of-the-surrogate, `NRSur7dq4Remnant_NN`. In this section we describe the `NRSur7dq4Remnant` structure and the relevant datasets. More details can be found in Ref. [59] and the supplemental material in Ref. [58]. The model represents a fit of 7 input parameters to 7 output parameters. The input parameters are the mass ratio, q , and dimensional spin components of the two pre-merger BHs, $\vec{\chi}_i$ with $i \in \{1, 2\}$, at a reference time $t = -100 M$ before merger¹ in the coorbital frame² (with M the binary’s total mass), while the 7 output parameters are the mass, m_f , spin, $\vec{\chi}_f$, and recoil velocity, \vec{v}_f , of the final BH. `NRSur7dq4Remnant` was

¹ Additional functionality allows for input spins specified at earlier frequencies and then evolved to $100 M$ before merger. We do not consider spin evolution here either in the fits or accuracy tests.

² In the coorbital frame the z -axis aligns with the orbital angular momentum, and the x -axis is defined as the direction from the smaller to the larger BH.

constructed through a separate GPR fit for each of its 7 output parameters, using a kernel given in Eq. (S3) of Ref. [58].

We then construct a neural network surrogate of `NRSur7dq4Remnant`. The output parameters are the same (remnant mass, spin, and velocity). For the input parameters, we use the mass ratio and spins in polar coordinates. Unlike Ref. [58], we do not reparametrize the spins to quantities motivated by post-Newtonian theory, as initial investigations suggest that the polar parameterization leads to the highest accuracy. Following Ref. [58], we standard-scale the input and output training data such that the mean is subtracted and the standard deviation re-scaled to 1, using `scikit-learn` [96]. Training is then based on fully-connected Multi-Layer Perceptron networks, with each layer (except the input and output ones) having the same number of neurons, as we find that this architecture is sufficiently complex for our target accuracy. We use `Tensorflow` for training and testing, though `gwbonsai` can alternatively utilize `PyTorch`.

We construct four datasets with `NRSur7dq4Remnant`: a training set with which to train the neural network, the \mathcal{T} -set; a validation set for use in training to avoid overfitting, the \mathcal{V} -set; a test set to evaluate the accuracy of the trained network, the \mathcal{S} -set; and a hold-out set, the \mathcal{H} -set. All sets comprise values for input parameters

$$\mathbf{X} = \{q, \chi_1, \theta_1, \phi_1, \chi_2, \theta_2, \phi_2\}, \quad (1)$$

and their corresponding output parameters

$$\mathbf{Y} = \{m_f, \vec{\chi}_f, \vec{v}_f\}. \quad (2)$$

The input spins are parameterized by their dimensionless spin magnitude $\chi_i = \|\chi_i\|$, spin tilt θ_i , and azimuthal angle ϕ_i measured at $t = -100 M$ before merger. The final mass is scaled to the total mass at the simulation relaxation time, and the remnant dimensionless spin and recoil velocity are expressed in Cartesian components. Input parameters \mathbf{X} lie within the boundaries of validity of `NRSur7dq4Remnant`, namely $q \in [1, 4]$, $\chi_i \leq 0.8$ and output parameters \mathbf{Y} are evaluated with `NRSur7dq4Remnant`.

We utilize two ways of selecting \mathbf{X} points. The first draws uniformly in

$$q \in [1, 4], \quad (3)$$

$$\chi_i \in [0, 0.8], \quad (4)$$

$$\theta_i \in [0, \pi], \quad (5)$$

$$\phi_i \in [0, 2\pi]. \quad (6)$$

The second is the sparse grid method presented in Appendix A of Ref. [56], from which we construct 1528 points, analogous to the 1528 points used to train `NRSur7dq4Remnant` in the first place. The validation \mathcal{V} -set and test \mathcal{S} -set are populated with 10,000 uniform draws. The holdout set \mathcal{H} -set is a combination of the 1528 sparse-grid points plus uniform draws up to a size

of 100,000 points. The initial training set \mathcal{T} -set is populated with the 1528 sparse-grid points and will iteratively be augmented by points from the \mathcal{H} -set.

The training loss function is the mean absolute error (L1 norm) over all output parameters,

$$\Delta = \frac{1}{n} \|\mathbf{Y}^{\text{tr}} - \mathbf{Y}^{\text{pr}}\|, \quad (7)$$

where n is the number of output parameters, \mathbf{Y}^{tr} is the vector of true values of the output parameters from `NRSur7dq4Remnant`, and \mathbf{Y}^{pr} are the predicted values. We monitor the loss over both training and validation sets during training and implement two conditions. Firstly, if the validation loss begins to monotonically increase for a period of 50 training epochs, we stop training and return the weights to when the validation loss was at its minimum. This prevents overfitting features in the training data that are not also representative of the validation data, and therefore of the parameter space region as a whole. Second, we implement a learning rate scheduler which reduces the learning rate by a factor of 10 whenever the training loss plateaus for a period of 50 epochs. Larger learning rates allow the neural network optimizer to make bigger adjustments to the weights with each training step, while a smaller learning rate encourages fine-tuning when the learnable parameters are close to a local minimum.

III. HYPERPARAMETER AND ARCHITECTURE OPTIMIZATION

In this section, we introduce a systematic approach to optimize the neural network architecture and hyperparameters through the hyperparameter optimization package `Optuna` [90], which uses a Tree-of-Parzen-Estimator [97] algorithm to update hyperparameter choices based on estimates of the final loss function evaluated on the unseen \mathcal{S} -set. We split the network optimization problem into two separate steps, first for the hyperparameters and second for the architecture (size and shape). We carry out the optimization separately for different configurations of output parameters: remnant mass (1D), remnant spin vector (3D), kick velocity (3D), remnant spin and kick velocity (6D), and all together (7D).

The optimization procedure of `Optuna` proceeds as follows. The algorithm draws initial samples of hyperparameter combinations from the prior of options given by the user, and trains these models. Based on the final loss values, it splits these samples into one “good” group of hyperparameter combinations and one “bad” group, and then uses kernel density estimators to model the probability distributions of these two groups. It then iteratively proposes new samples that maximize the ratio of the “good” probability distribution to the “bad” one, evaluating these new models and updating the groups. The `Optuna` algorithm further relies on a number of hyperparameters, including: the prior weights for hyperpa-

Configuration	Activation Function	Weight Initialization	Normalization	Optimizer	Initial Learning Rate	Optimal Final Loss	Final Loss Standard Deviation
Mass	Softplus	HeNormal	No	Adam	2.0×10^{-4}	1.5×10^{-3}	2.6×10^{-1}
Spins	Elu	glorot uniform	No	Nadam	2.0×10^{-4}	1.1×10^{-2}	2.6×10^{-1}
Velocities	Elu	glorot uniform	No	Adam	5.0×10^{-4}	4.0×10^{-2}	2.2×10^{-1}
6D	Softplus	HeNormal	No	Nadam	5.0×10^{-4}	1.9×10^{-2}	2.3×10^{-1}
7D	Softplus	glorot uniform	No	Nadam	1.0×10^{-3}	1.8×10^{-2}	2.4×10^{-1}

TABLE I. Results for the functional hyperparameter optimization. We consider networks for different configurations of output parameters and list the optimal choice or value of each hyperparameter. We also list the optimal loss achieved as well as the standard deviation of final losses across the hyperparameter optimization stage.

Configuration	Hidden Layers	Neurons per Layer	Batch Size	Dropout	Optimal Final Loss	Final Loss Standard Deviation
Mass	3	10	64	No	2.0×10^{-4}	3.0×10^{-2}
Spins	5	200	256	No	1.1×10^{-2}	9.7×10^{-2}
Velocities	8	50	128	No	1.8×10^{-2}	1.2×10^{-1}
6D	5	100	128	No	1.8×10^{-2}	1.3×10^{-1}
7D	5	100	128	No	1.7×10^{-2}	1.2×10^{-1}

TABLE II. Same as Table I but for the network architecture and specifically the size and shape parameters.

rameters; the number of startup trials which are sampled randomly from the prior; the number of trials run; and the number of samples used to calculate the expected improvement, which is then maximized to choose the next samples. Configuration files for our analyses listing all choices are available at [89].

We begin with the functional hyperparameters as their impact on the fit is more complex, while fixing the size and shape parameters. We fix the number of hidden layers to 4 with no dropout layers, neurons per layer to 100, and batch size to 128 (more details about the role of these parameters are provided later). We also use a fixed training set size of 10,000 points. We study the effect of the functional hyperparameters as follows. Note that these functional hyperparameters are optimized over simultaneously in this step.

- (i) The *activation function* is applied to data passing across each neuron in the hidden layers, and adds non-linearity to the network which allows it to universally approximate functions. Different activation functions and their gradients (which need to be stable and easy to compute) will work better for different problems, and we consider: `relu`, `sigmoid`, `softplus`, `softsign`, `tanh`, `selu`, `elu`, `exponential`, and `LeakyReLU`.
- (ii) *Weight initialization* assigns initial values to the weights of neurons based on a distribution, and acts as a seed for training. A suitable choice of weight initialization can allow for faster and more stable training by addressing vanishing or exploding gradients, and we consider a choice of `Glorot uniform`, `HeNormal` and `HeUniform` distributions.
- (iii) We consider whether to add a *normalization layer*

within the network, which scales the inputs to zero mean and unit variance. Though we scale the input and output training data in the same way, renormalization in the middle of the network can help stabilize the gradients of the activation function and allow for smoother training.

- (iv) The *optimizer* is the algorithm that updates the neuron weights during training; we explore: `Adam`, `Adamax`, `Nadam`, and `Ftrl`.
- (v) While we use an adaptive learning rate as described in Sec. II, we consider the *initial learning rate* to adjust how aggressive the initial training adjustments are, allowing a discrete set of values: $[1 \times 10^{-5}, 2 \times 10^{-5}, 5 \times 10^{-5}, 1 \times 10^{-4}, 2 \times 10^{-4}, 5 \times 10^{-4}, 1 \times 10^{-3}]$.

Results for the hyperparameter optimization are shown in Table I. For each configuration of output parameters, we list the optimal choice of hyperparameter, the resulting optimal final loss, and the standard deviation of losses across the functional hyperparameter optimization stage. The final loss for the optimal configuration is similar for all configurations other than the mass-only network, for which it is a factor of 10 lower, likely because it is the simplest one. For all configurations, the optimal loss is around an order of magnitude lower than the standard deviation, indicating that the optimization process indeed found a well-performing minimum setting.

With the optimal functional hyperparameters from Table I, we turn to the network architecture and specifically the size and shape parameters of the network layers. For this relatively simple regression problem, we restrict to a fully-connected multi-layer perceptron with all layers the same size.

- (i) Qualitatively speaking, the *number of neurons per layer* corresponds to the number of “features” we expect in the data, and the *number of hidden layers* to how complex those features are. Optimizing over these parameters is crucial for avoiding over- and under-fitting. We consider layer sizes between 10 and 200 neurons and the number of hidden layers between 2 and 12 (excluding input, output, normalization, and dropout layers).
- (ii) The *batch size*, which is the number of points passed to the network simultaneously during training, impacts the tendency to over-fit if too small. We consider values in powers of 2 between 64 and 512.
- (iii) We explore the impact of a *dropout layer*, which probabilistically discards neuron information during training. Dropout layers can help avoid over-fitting, so we optimize over whether to include one, and what dropout probability it has, with a uniform prior between 0 and 1.

Results for the network architecture optimization step for each configuration of output parameters is shown in Table II. The optimal final losses and standard deviations are again relatively similar for all configurations except the mass-only one. The optimal losses are still around an order of magnitude lower than the standard deviations.

The optimization results of Tabs. I and II elucidate the role of the various settings as well as the structure of the problem. Many results are similar for the different output configurations, indicating that they are the generally preferred settings. For example, none of the configurations benefit from a normalization or dropout layer, and all configurations are best trained with an Adam optimizer or its closely related variant Nadam, which uses the Adam algorithm with Nesterov momentum to correct for overly large gradient jumps. The preferred activation functions are `softplus`, which is a smooth approximation to the often-used `relu`, and `elu`, which is also similar to the `relu` activation but allowing for negative values of neuron output which can speed up learning. The optimal weight initialization distribution is a mixture of the commonly used `glorot uniform` and `HeNormal`, which is suited to `relu` and related activation functions [98].

The optimal solutions given in Table I are relatively stable to the choice of activation function, as throughout sampling the optimal activation function generally led to lower final losses even as other functional hyperparameters varied. The performance of different weight initialization and optimizer settings were more dependent on other hyperparameters, and the Adam and Nadam optimizers performed similarly for all configurations. We also found a positive correlation between the batch size and number of neurons per layer. This is expected, as larger layers will need more information to update their weights and train efficiently.

Differences between the optimal hyperparameters for the different configurations further reveal information

Configuration	Training Points	Epochs	Final Loss
Mass	15,000	5,100	6.4×10^{-5}
Spins	30,000	4,320	5.3×10^{-5}
Velocities	45,000	6,086	4.6×10^{-5}
6D	30,000	5,883	5.0×10^{-5}
7D	20,000	6,003	4.5×10^{-5}

TABLE III. Settings and performance of the final networks for each configuration of output parameters. Besides the optimal hyperparameters and architecture listed in Tables I and II respectively, here we list the optimal training size, determined in Sec. IV, the training epochs, and the final loss achieved.

about the properties of the parameter space. The remnant spin configuration requires the most neurons per layer and the largest batch size, suggesting a feature-rich parameter space. The kick velocity optimizes to the largest number of hidden layers, suggesting more complex features to fit. However, when spin and velocity are combined together in a single 6D configuration, or as part of the full 7D network, this complexity is reduced, suggesting that the different output parameters are related to each other. The mass-only configuration is the least feature-rich, requiring the fewest and smallest layers, and the smallest batch size. This result is expected given that the final mass is always close to 1, further highlighting the sensibility of the optimization framework. Finally, all configurations except the full 7D one are optimized with a medium-valued initial learning rate of $2 - 5 \times 10^{-4}$, while the full 7D configuration benefits from a larger initial learning rate of 1×10^{-3} for bigger weight adjustments.

IV. TRAINING DATASET SIZE OPTIMIZATION

Having selected values for the network size and shape as well as the functional hyperparameters, we now assess how much training data is required. We follow an iterative approach:

1. Begin with a training \mathcal{T} -set containing the 1528 sparse-grid points.
2. Train a neural network for 2,000 epochs, chosen to balance computational cost with obtaining representative results.
3. Evaluate the fit accuracy on the holdout \mathcal{H} -set and test \mathcal{S} -set sets.
4. Choose the worst performing points from the \mathcal{H} -set and add them to the \mathcal{T} -set (up to next multiple of 500, or next multiple of 5,000 if more than 10,000 training points).
5. Retrain the neural network.
6. Repeat steps 2-5 until \mathcal{T} -set= \mathcal{H} -set.

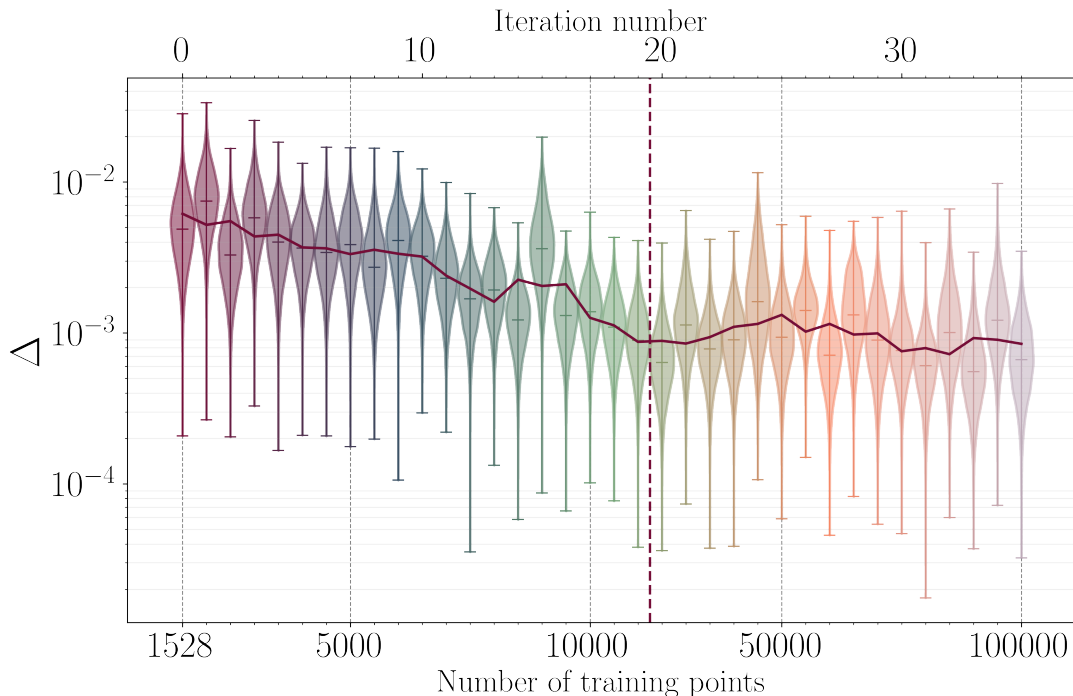


FIG. 1. Distribution of the mean error Δ over the unseen \mathcal{S} -set (violins) as a function of the training dataset size for the 7D configuration network and the training procedure detailed in Sec. IV. As the number of training points increases, the mean error tends to decrease and plateaus after around 19 iterations (dashed line). In purple solid, we show the running mean over three iterations of the median error, which we use to assess where the plateau begins. We select 20,000 points (roughly the size of the 19th iteration) as the optimal training dataset size.

Figure 1 shows the distribution of mean error Δ , Eq. (7), for the \mathcal{S} -set for the 7D network configuration; we obtain qualitatively similar trends for other configurations. The mean error overall improves with increasing size of the training set, as the violins trend downwards with each iteration. The running mean of the median Δ over 3 iterations plateaus after ~ 19 iterations, indicating diminishing returns from further increasing the amount of training data. We, therefore, identify 20,000 points as the optimal training size for this configuration.

We repeat this process for all network configurations and identify a training dataset size that balances accuracy with training cost. Results are shown in Table III. The mass-only configuration reaches the loss plateau with the smallest amount of training data. This is consistent with the findings of Sec. III that the final mass is the simplest to train, requiring the lightest network settings. On the other side, the kick velocity requires the most training data, to represent the complexity of the parameter space features, again consistent with Sec. III. Interestingly, again the full 7D configuration network requires fewer points (lighter settings) than the technically lower-dimensional networks for the spins and/or velocities. This again suggests that including all parameters in a single network adds information that simplifies the problem. Even in this case, however, the training size required, $\mathcal{O}(10^4)$, is about an order of magnitude higher

than the size of current NR catalogs and the training size of the original surrogate `NRSur7dq4Remnant`, $\mathcal{O}(10^3)$.

Figure 1 and Table III quote the mean error over all output parameters for a given configuration. We further examine the mean error for subsets of the output parameters of each configuration, for example, the final mass, remnant spin magnitude or angle, and kick velocity magnitude or angle, as appropriate. Interestingly, we find that the training dataset size at which the loss plateaus is independent of which output parameters we consider. This suggests that there is an optimal training dataset for all output parameters and which improves the network accuracy as a whole.

The iterative addition of training data further allows us to explore which regions of the parameter space contribute to the loss of accuracy. Figure 2 shows the points that get added to the training set. The top row shows the mean error Δ for the 1,000 worst-performing points across the \mathcal{T} -set after 10 iterations. The worst-performing points are concentrated in areas with high mass ratios and spin magnitudes. These 1,000 points are then added to the training dataset for the next iteration. In the bottom row, we show the same mean error but for the 1,000 worst-performing points in the \mathcal{T} -set after 19 iterations (which is where the plateau in improvement in Fig. 1 occurs). The worst-performing points are more evenly spread throughout the param-

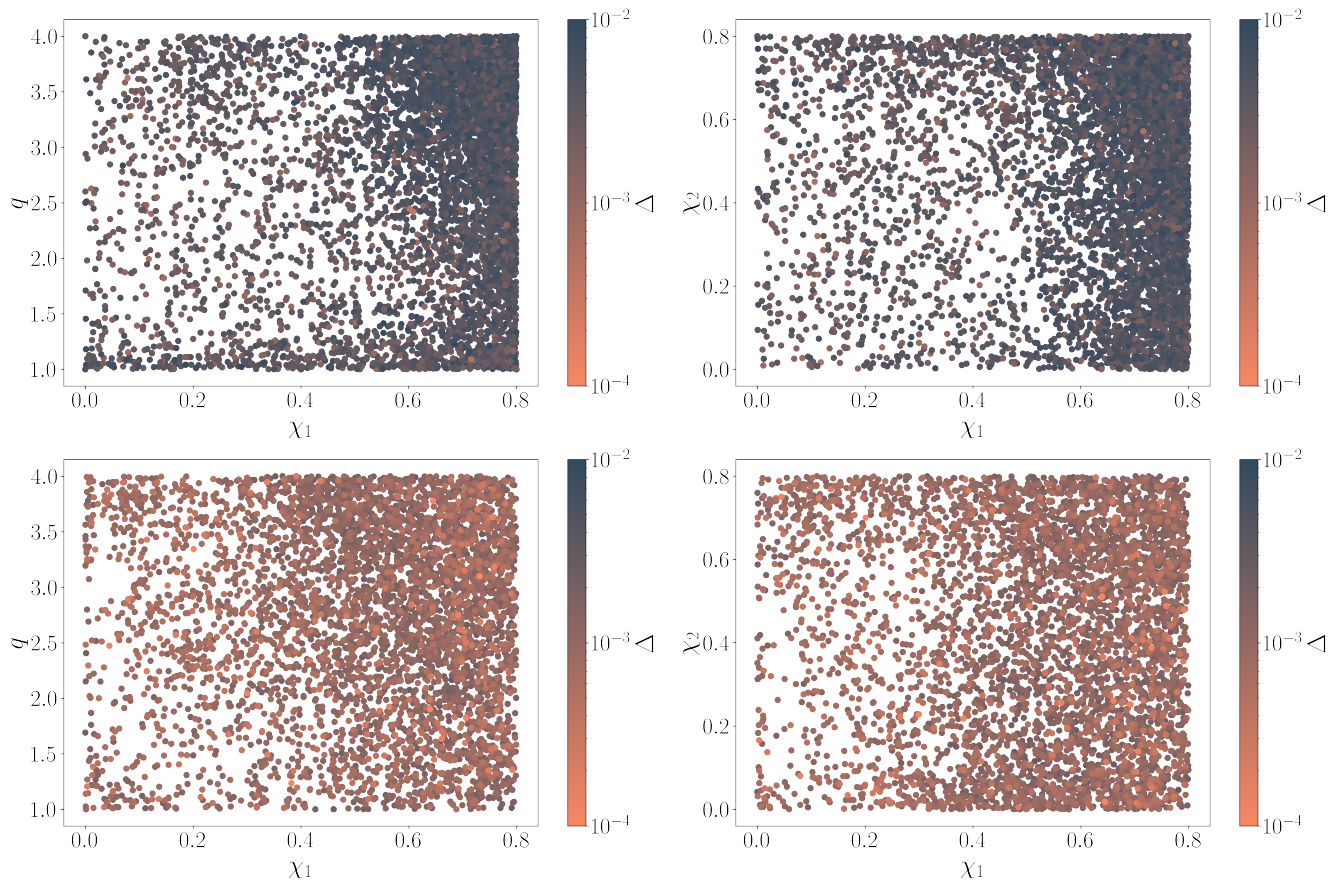


FIG. 2. Distribution of the 1,000 worst-performing points in the \mathcal{T} -set across the parameters in mass ratio-primary spin magnitude (left column) and spin magnitudes (right column) for the full 7D configuration after 10 (top row) and 19 (bottom row) iterations. Each point is colored by its mean error Δ . These points are not part of the training set for their respective iteration, but are then added to the training set for the next iteration. The 10th iteration worst-performing points are concentrated in the high mass ratio and large spin magnitude areas. By the 19th iteration (where the performance plateau occurs), the worst-performing points are distributed across a wider range of spin magnitudes in the training region, more evenly in mass ratios, and with lower mean errors. This suggests that the iterative enrichment of the training set effectively samples the parameter space by dynamically selecting the most representative points.

ter space and the mean errors are lower overall. This suggests that the iterative procedure for adding training data identifies problematic parameter space regions and efficiently fills them up. By the time the performance plateau is reached, errors are not only reduced but also more evenly distributed across parameters.

V. FINAL MODEL EVALUATION

Having optimized the network architecture, hyperparameters, and training dataset size, we now train the final models for each configuration of output parameters. Specifically, we use the hyperparameters and size and shape parameters listed in Tables I and II respectively and the training dataset size in Table III. We use an adaptive learning rate and the early stopping condition described in Sec. II; the resulting final number of training epochs is in Table III. Also listed in Table III is

the final loss achieved after each network is fully trained. We obtain comparable losses for each configuration, with the 7D configuration performing marginally better. Coupled to the simpler settings in Tables I and II, we therefore conclude that the 7D configuration is preferred and present results only for this network in what follows, which we label as `NRSur7dq4Remnant_NN`.

The accuracy of `NRSur7dq4Remnant_NN` is assessed in Fig. 3. We plot the distribution of errors across the unseen \mathcal{S} -set for output parameters defined as

$$\Delta m_f = \left| m_f^{\text{tr}} - m_f^{\text{pr}} \right|, \quad (8)$$

$$\Delta x = \left| \vec{x}^{\text{tr}} - \vec{x}^{\text{pr}} \right|, \quad (9)$$

$$\Delta \theta_x = \cos^{-1} \left(\hat{x}^{\text{tr}} \cdot \hat{x}^{\text{pr}} \right), \quad (10)$$

where \vec{x} represents either of the vectors $\vec{\chi}_f$ or \vec{v}_f , and true and predicted values refer to `NRSur7dq4Remnant` and `NRSur7dq4Remnant_NN` respectively. We also plot the medians and 95th percentiles of these distributions as solid

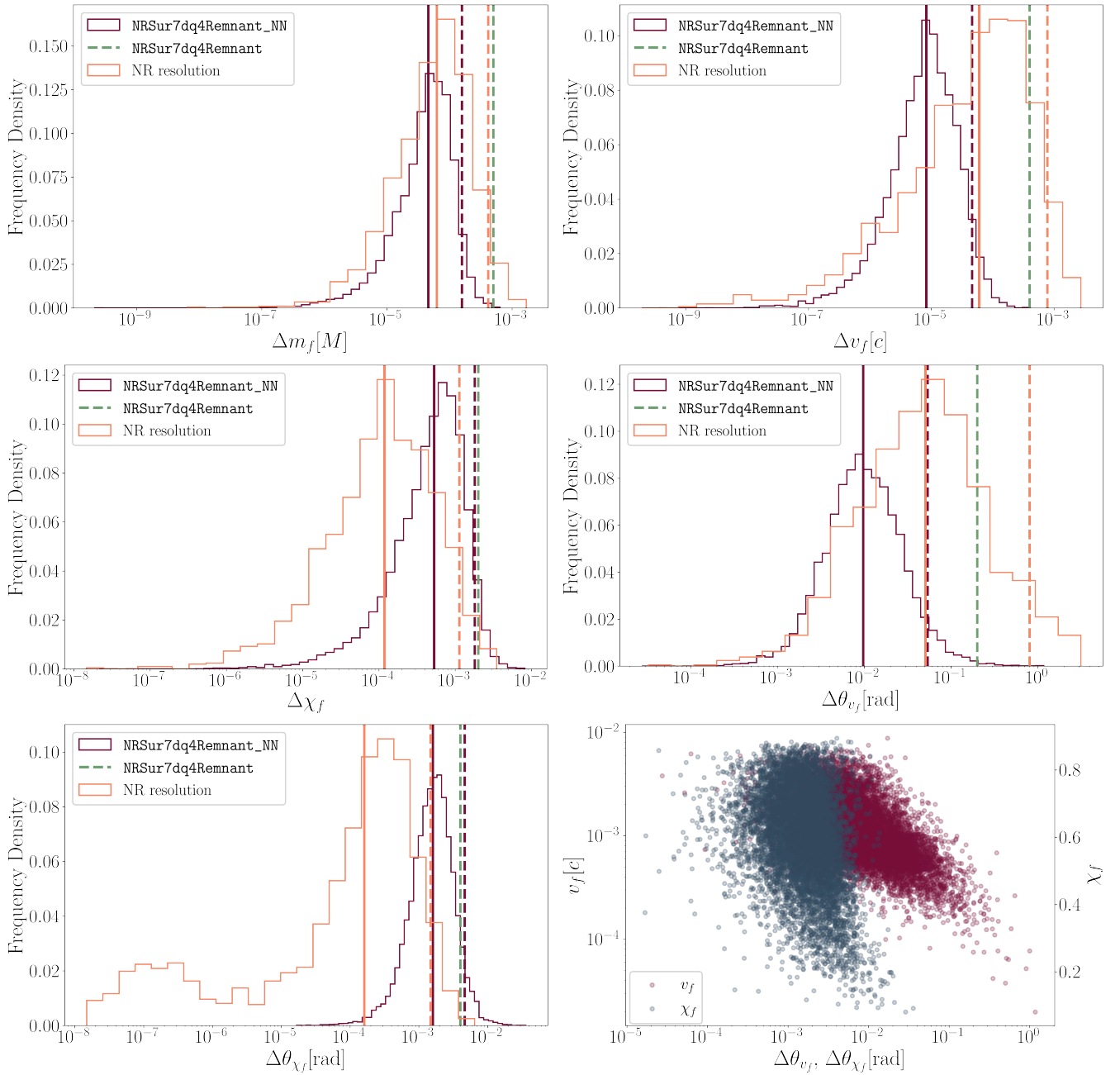


FIG. 3. Errors over the \mathcal{S} -set for the remnant mass, Δm_f , kick magnitude, Δv_f , spin magnitude, $\Delta \chi_f$, kick direction $\Delta \theta_{v_f}$, and spin direction, $\Delta \theta_{\chi_f}$. Besides error histograms, in the bottom right panel we also show the joint distribution of magnitude and direction errors for both the kick velocity (purple) and spin vectors (blue). Results histograms for **NRSur7dq4Remnant_NN** compared to the **NRSur7dq4Remnant** surrogate it was trained on are shown in purple, with medians (solid) and 95th percentiles (dashed) shown as purple vertical lines. Green dashed vertical lines indicate the 95th percentile errors of **NRSur7dq4Remnant** with respect to the NR it is built upon; these errors are sometimes larger than the reported **NRSur7dq4Remnant_NN** errors as the latter is compared with **NRSur7dq4Remnant** instead of NR. We also show the distributions of NR resolution errors in orange, with medians (solid) and 95th percentiles (dashed) shown as vertical orange lines.

and dashed purple vertical lines, respectively, and the 95th percentiles of the errors of **NRSur7dq4Remnant** with respect to the underlying NR data it is based on as dashed green vertical lines. We list these 95th error percentiles in Table IV. For reference, we also

plot the resolution error of the NR simulations that **NRSur7dq4Remnant** was based on (computed from the two highest NR resolutions available). Due to different frame choices when computing the resolution errors, our resolution errors differ slightly from Ref. [59]. Here, we

use the publicly-available metadata [19] to compute errors in the initial frame of the simulations, whereas in Ref. [59] the resolutions are rotated into a frame which aligns with the coorbital frame $100M$ before merger at the time where the input masses and spins are measured. Similar to `NRSur7dq4Remnant` in Ref. [59], the NR resolution errors are comparable or slightly higher than the surrogate model errors for the remnant mass and kick velocity magnitude and direction, suggesting that the surrogate building is not a dominant source of error. For the remnant spin quantities, the resolution errors are lower than those of our model. The distribution of errors over the \mathcal{S} -set is similar to errors calculated over the larger \mathcal{T} -set, suggesting that the \mathcal{S} -set is sufficiently dense to quantify the errors over the 7D space.

Compared to `NRSur7dq4Remnant` that it was trained on, `NRSur7dq4Remnant_NN` is extremely accurate. For the final mass and recoil velocity, the 95th percentiles of `NRSur7dq4Remnant_NN` are less than those of `NRSur7dq4Remnant`. For the kick velocity magnitude specifically, the 95th percentile error is almost an order of magnitude less than `NRSur7dq4Remnant`. We also find improvements of roughly a factor of 3 and 2 in the remnant mass error and kick velocity direction, respectively. For the final spin, the errors are comparable. This suggests that `NRSur7dq4Remnant_NN` incurs only minimal additional errors on top of those of `NRSur7dq4Remnant`.

In the bottom right panel of Fig. 3, we show a scatter plot of the remnant spin magnitude χ_f against the spin direction error $\Delta\theta_{\chi_f}$ (left y -axis), and the kick velocity magnitude v_f against the kick direction error $\Delta\theta_{v_f}$ (right y -axis). Reference [59] reported a larger angular error for larger kick velocity magnitudes; we confirm this result and extend it to the spin vector. This is likely because larger magnitude vectors are easier to fit, as our loss function is the mean error over the Cartesian vector coordinates. Therefore, a larger error in angle for a smaller magnitude vector will have less of an impact on the overall loss.

Having verified the accuracy of `NRSur7dq4Remnant_NN`, we now turn to its evaluation performance. We start with CPU timing tests using an Apple M2 chip with 8 cores. In Fig. 4 we compare evaluation times over the \mathcal{S} -set for the following implementations. For `NRSur7dq4Remnant_NN`, we consider the native `Tensorflow` architecture and also a `NumPy` matrix implementation, where we take the final network weights and biases, and apply them to layers of a `NumPy` array, also using `NumPy` implementations of the relevant activation function in between. We additionally consider a `JAX` implementation, where similarly to the `NumPy` implementation, the weights and biases are applied to a `JAX` array with `JAX` activation functions. For `NRSur7dq4Remnant`, we consider the implementations in `surfinBH` [99] and in `LALSimulation` [100]. Between the `NRSur7dq4Remnant` implementations, the one in `LALSimulation` is faster with a median evaluation time of 5.6×10^{-4} s compared to the `surfinBH` one at 3.5×10^{-3} s. We obtain a median evaluation time

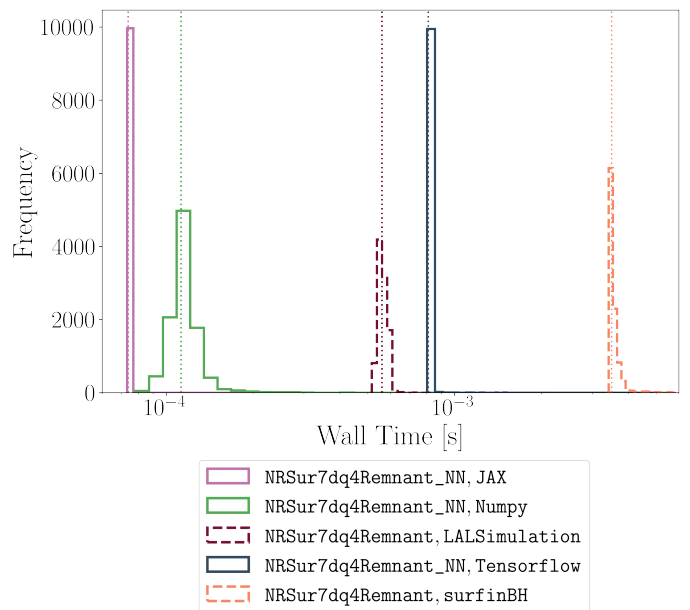


FIG. 4. Evaluation timing comparison on a single CPU of `NRSur7dq4Remnant` (orange and purple) against `NRSur7dq4Remnant_NN` (pink, green and blue), over the unseen \mathcal{S} -set. The dashed vertical lines show the median for each distribution. For each surrogate model, we further consider multiple implementations; see text for details. We find a runtime speedup of around an order of magnitude with the `JAX` implementation, to a median of 7.4×10^{-5} s, while a `NumPy` implementation achieves a median time of 1.1×10^{-4} s, and the native `Tensorflow` implementation a median time of 8.1×10^{-4} s. The median evaluation times for the `NRSur7dq4Remnant` model are 3.5×10^{-3} s and 5.6×10^{-4} s for the `surfinBH` and `LALSimulation` implementations respectively.

of 7.4×10^{-5} s with `JAX`, 1.1×10^{-4} s with `NumPy` and 8.1×10^{-4} s with `Tensorflow`.³ Therefore, the neural network-based model represents a speed up of nearly an order of magnitude with the `JAX` implementation.

As the neural network is designed to be efficiently evaluated in batch, we also test the native `Tensorflow` implementation as a function of batch size using an NVIDIA A100-SXM4-40GB GPU. We draw points uniformly from the training parameter space and evaluate the model in batch sizes up to 10^7 points. Figure 5 shows the speedup, defined as the batch size divided by the evaluation time, as a function of batch size. As the batch size increases, so does the speedup up to a batch size of 10^5 , after which all of the GPU processing units have been utilized. Even larger batches must be evaluated sequentially in units

³ `Tensorflow` evaluates slower than a simpler `JAX` or `NumPy` implementation without GPU parallelization due to the overhead costs of performing operations on tensor objects as opposed to arrays. Differences in framework construction may mean these overheads are lessened with other backends, for example `PyTorch`.

Error Quantity	NRSur7dq4Remnant_NN 95th Percentile	NRSur7dq4Remnant 95th Percentile	NR Resolution Error 95th Percentile
$\Delta m_f [M]$	1.6×10^{-4}	5×10^{-4}	4.1×10^{-4}
$\Delta \chi_f$	1.8×10^{-3}	2×10^{-3}	1.1×10^{-3}
$\Delta \theta_{\chi_f} [\text{rad}]$	4.6×10^{-3}	4×10^{-3}	1.5×10^{-3}
$\Delta v_f [c]$	4.6×10^{-5}	4×10^{-4}	7.8×10^{-4}
$\Delta \theta_{v_f} [\text{rad}]$	5.4×10^{-2}	2×10^{-1}	8.0×10^{-1}

TABLE IV. 95th percentile errors as shown by the dashed vertical lines in Fig. 3. The first column shows the errors of NRSur7dq4Remnant_NN with respect to NRSur7dq4Remnant, the second column shows the errors of NRSur7dq4Remnant with respect to the underlying NR simulations, and the final column shows the NR resolution errors calculated between the two highest resolution levels.

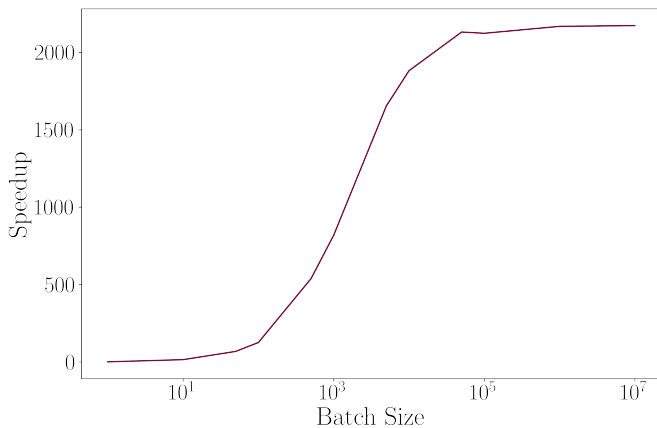


FIG. 5. Evaluation timing on an NVIDIA A100-SXM4-40GB GPU of the `Tensorflow` NRSur7dq4Remnant_NN implementation, comparing speedups as a function of batch size due to efficient parallel processing. The speedup is defined as the batch size divided by the evaluation time. We find a significant speed up compared to single-point evaluation as the batch size increases up to 10^5 points, after which the speed up plateaus.

of 10^5 , so the speed up remains constant. The maximum speed up from batch evaluation exceeds 3 orders of magnitude. Combined with the speed up just from the CPU evaluation, it leads to an overall potential maximum speed up of around 4–5 orders of magnitude between the original surrogate model and its neural network version.

Lastly, we test how the model extrapolates outside its parameter space training region. Extrapolation from $q = 4$ to 6 was considered in Ref. [59] and here we also consider spin. In this test, the ground truth model remains NRSur7dq4Remnant rather than NR. This test is therefore assessing how NRSur7dq4Remnant_NN extrapolates over NRSur7dq4Remnant, rather than its accuracy in reproducing NR data in that domain. We draw uniformly 1,000 with only mass ratio extrapolation, $q \in [4, 6]$, 500 points with only primary spin magnitude extrapolation, $\chi_1 \in [0.8, 1.0]$, and a further 250 points where both the mass ratio and primary spin magnitude are extrapolated, $q \in [4, 6]$, $\chi_1 \in [0.8, 1.0]$. For reference, we

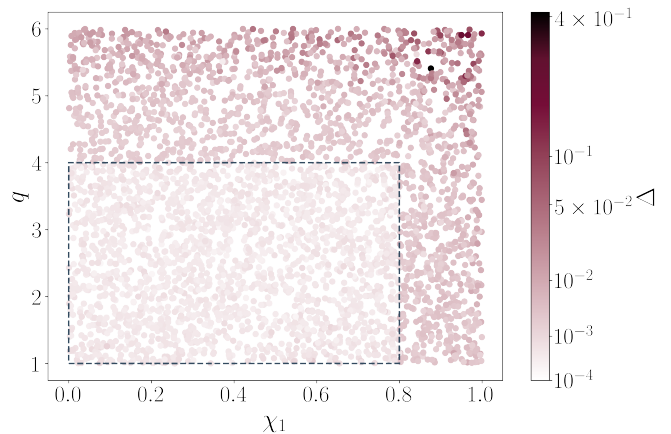


FIG. 6. Random points on the $q - \chi_1$ plane colored by their mean error Δ . The dashed rectangle denotes the training region, $q \in [1, 2]$, $\chi_1 \in [0, 0.8]$. Points outside the rectangle are extrapolated at mass ratio $q \in [4, 6]$ and primary spin magnitudes $\chi_1 \in [0.8, 1.0]$. The mean error is higher across the extrapolation regions than across the training region. The spin magnitudes extrapolate more accurately than the mass ratio, and the worst-performing points have near-maximal spin magnitude and q close to 6.

also consider 1,000 points from the \mathcal{S} -set, namely from within the training region. We evaluate these points with NRSur7dq4Remnant_NN and plot them in the q and χ_1 space, colored by the mean error Δ . The results are shown in Figure 6. Across the training region (denoted by the dashed rectangle), the mean errors are fairly uniform and around 10^{3-4} , consistent with Fig. 3. As the mass ratio and/or spin magnitude increases outside this region, the mean errors increase rapidly. Mean errors for extrapolated spin magnitudes remain fairly consistent as long as the mass ratio stays within its training region, never exceeding 4×10^{-2} . The extrapolated mass ratio region (with the spin remaining less than 0.8) sees larger errors, with $q \sim 6$ resulting in errors up to 2×10^{-1} . The worst errors are for points where both the mass ratio and spin magnitude are extrapolated, with errors for maximal spins and mass ratios reaching up to 3×10^{-1} . These results suggest that extrapolation along mass ratio

is more perilous than along spin magnitude and further NR simulations with unequal masses are required to improve surrogate models.

VI. CONCLUSIONS

In this work, we have developed a systematic approach to optimizing the hyperparameters and training datasets of neural network surrogate models. We have applied our methodology to BBH remnant properties, building a new model, `NRSur7dq4Remnant_NN`, based on training data from the existing `NRSur7dq4Remnant` model. We achieve comparable accuracy with respect to the underlying model to the accuracy of `NRSur7dq4Remnant` to its underlying NR simulations for the remnant mass and final spin vector. The accuracy for the recoil velocity is about an order of magnitude higher.

`NRSur7dq4Remnant_NN` evaluates faster than the `surfinBH` implementation of `NRSur7dq4Remnant` on a single CPU when using the native `Tensorflow` architecture, with a median speedup of 4.3 times, but performs slower than the `LALSimulation` implementation, by a factor of 1.4. We achieve greater speedups when using a `Numpy` implementation, improving to speedup factors of 5 and 31 compared to `LALSimulation` and `surfinBH` respectively. Our greatest speedups are obtained using a `JAX` implementation, by 8 and 47 times compared to `LALSimulation` and `surfinBH` respectively. When evaluating in batch on a GPU, we obtain additional speedups up to 2000 times, resulting in an overall maximum speedup of ~ 4 orders of magnitude.

These accuracies and speedups, however, come at the expense of an order of magnitude more training data than the available NR catalogs. We therefore propose such neural network-based surrogates as a secondary step after initially building an NR surrogate using different methods. The neural network-based surrogate can then unlock significant speedups without compromising accuracy. Our method is applicable to waveform surrogates as well as remnant properties, and we leave this application to future work. While we have used neural networks in a secondary NR surrogate-building stage, an alternative could be to use transfer learning from a neural network surrogate of a different model, for example an effective-one-body model, where training data is more readily available. In this alternative approach, the neural network surrogate would then be fine-tuned on the smaller pool of NR waveforms, and we leave investigations of this method to future work.

Such future work could also explore further improve-

ments. Firstly, we do not explore the impact of re-parameterization of the training data. Through initial investigations, we find that binary spins are more easily fitted when expressed in spherical rather than Cartesian coordinates. We do not explore further techniques, such as principle component analyses or dimensional reduction, which might be useful for waveform surrogates where the training data have many more dimensions. Secondly, we also do not consider the evolution of input parameters to different reference frequencies, instead performing our fit at the same reference time (100 M before merger) as with the original `NRSur7dq4Remnant` model. Thirdly, one limitation of the neural network is that it does not provide fitting error estimates in the same way as GPR fitting does. Therefore we can only assess model accuracy from the errors with respect to `NRSur7dq4Remnant` over a pre-defined test set.

Finally, the optimization procedure is not guaranteed to achieve a global minimum in the final loss, especially since we split optimization into distinct stages: functional hyperparameter, size and shape parameters, and training dataset. Additionally, because each sample neural network in the optimization is initialized using a single random seed, there is a chance that the globally optimal configuration underperforms with this seed and is discarded. However, it will achieve a local minimum, which we assume to be sufficient (and indeed confirm so for `NRSur7dq4Remnant_NN`), and it is guaranteed to finish in a finite time. If global accuracy is required for future surrogate models, optimization could be done with several seed points in parallel, for a better chance of reaching the true global minimum loss.

`NRSur7dq4Remnant_NN` is publicly available at [99] and `gwbonsai` at [89].

ACKNOWLEDGMENTS

LMT is supported by NSF MPS-Gravity Award 2207758 and by NSF Grant 2309200. KC was supported by NSF Grant PHY-2409001. V.V. acknowledges support from NSF Grant No. PHY-2309301. S.E.F. acknowledges support from NSF Grants PHY-2110496 and AST-2407454. S.E.F. and V.V. were supported by UMass Dartmouth’s Marine and Undersea Technology (MUST) research program funded by the Office of Naval Research (ONR) under grant no. N00014-23-1-2141. The authors are grateful for computational resources provided by the LIGO Laboratory and supported by National Science Foundation Grants PHY-0757058 and PHY-0823459.

[1] B. P. Abbott *et al.* (LIGO Scientific, Virgo), “GWTC-1: A Gravitational-Wave Transient Catalog of Compact Binary Mergers Observed by LIGO and Virgo during

the First and Second Observing Runs,” *Phys. Rev. X* **9**, 031040 (2019), [arXiv:1811.12907](https://arxiv.org/abs/1811.12907) [astro-ph.HE].

- [2] R. Abbott *et al.* (LIGO Scientific, Virgo), “GWTC-2: Compact Binary Coalescences Observed by LIGO and Virgo During the First Half of the Third Observing Run,” *Phys. Rev. X* **11**, 021053 (2021), [arXiv:2010.14527 \[gr-qc\]](#).
- [3] R. Abbott *et al.* (LIGO Scientific, VIRGO), “GWTC-2.1: Deep extended catalog of compact binary coalescences observed by LIGO and Virgo during the first half of the third observing run,” *Phys. Rev. D* **109**, 022001 (2024), [arXiv:2108.01045 \[gr-qc\]](#).
- [4] R. Abbott *et al.* (KAGRA, VIRGO, LIGO Scientific), “GWTC-3: Compact Binary Coalescences Observed by LIGO and Virgo during the Second Part of the Third Observing Run,” *Phys. Rev. X* **13**, 041039 (2023), [arXiv:2111.03606 \[gr-qc\]](#).
- [5] Alexander H. Nitz, Collin Capano, Alex B. Nielsen, Steven Reyes, Rebecca White, Duncan A. Brown, and Badri Krishnan, “1-OGC: The first open gravitational-wave catalog of binary mergers from analysis of public Advanced LIGO data,” *Astrophys. J.* **872**, 195 (2019), [arXiv:1811.01921 \[gr-qc\]](#).
- [6] Alexander H. Nitz, Thomas Dent, Gareth S. Davies, Sumit Kumar, Collin D. Capano, Ian Harry, Simone Mozzon, Laura Nuttall, Andrew Lundgren, and Márton Tápai, “2-OGC: Open Gravitational-wave Catalog of binary mergers from analysis of public Advanced LIGO and Virgo data,” *Astrophys. J.* **891**, 123 (2020), [arXiv:1910.05331 \[astro-ph.HE\]](#).
- [7] Alexander H. Nitz, Collin D. Capano, Sumit Kumar, Yi-Fan Wang, Shilpa Kastha, Marlin Schäfer, Rahul Dhurkunde, and Miriam Cabero, “3-OGC: Catalog of Gravitational Waves from Compact-binary Mergers,” *Astrophys. J.* **922**, 76 (2021), [arXiv:2105.09151 \[astro-ph.HE\]](#).
- [8] Alexander H. Nitz, Sumit Kumar, Yi-Fan Wang, Shilpa Kastha, Shichao Wu, Marlin Schäfer, Rahul Dhurkunde, and Collin D. Capano, “4-OGC: Catalog of Gravitational Waves from Compact Binary Mergers,” *Astrophys. J.* **946**, 59 (2023), [arXiv:2112.06878 \[astro-ph.HE\]](#).
- [9] Tejaswi Venumadhav, Barak Zackay, Javier Roulet, Liang Dai, and Matias Zaldarriaga, “New search pipeline for compact binary mergers: Results for binary black holes in the first observing run of Advanced LIGO,” *Phys. Rev. D* **100**, 023011 (2019), [arXiv:1902.10341 \[astro-ph.IM\]](#).
- [10] Tejaswi Venumadhav, Barak Zackay, Javier Roulet, Liang Dai, and Matias Zaldarriaga, “New binary black hole mergers in the second observing run of Advanced LIGO and Advanced Virgo,” *Phys. Rev. D* **101**, 083030 (2020), [arXiv:1904.07214 \[astro-ph.HE\]](#).
- [11] Seth Olsen, Tejaswi Venumadhav, Jonathan Mushkin, Javier Roulet, Barak Zackay, and Matias Zaldarriaga, “New binary black hole mergers in the LIGO-Virgo O3a data,” *Phys. Rev. D* **106**, 043009 (2022), [arXiv:2201.02252 \[astro-ph.HE\]](#).
- [12] Ajit Kumar Mehta, Seth Olsen, Digvijay Wadekar, Javier Roulet, Tejaswi Venumadhav, Jonathan Mushkin, Barak Zackay, and Matias Zaldarriaga, “New binary black hole mergers in the LIGO-Virgo O3b data,” (2023), [arXiv:2311.06061 \[gr-qc\]](#).
- [13] J. Aasi *et al.* (LIGO Scientific), “Advanced LIGO,” *Class. Quant. Grav.* **32**, 074001 (2015), [arXiv:1411.4547 \[gr-qc\]](#).
- [14] F. Acernese *et al.* (VIRGO), “Advanced Virgo: a second-generation interferometric gravitational wave detector,” *Class. Quant. Grav.* **32**, 024001 (2015), [arXiv:1408.3978 \[gr-qc\]](#).
- [15] T. Akutsu *et al.* (KAGRA), “Overview of KAGRA: Detector design and construction history,” *PTEP* **2021**, 05A101 (2021), [arXiv:2005.05574 \[physics.ins-det\]](#).
- [16] Curt Cutler and Eanna E. Flanagan, “Gravitational waves from merging compact binaries: How accurately can one extract the binary’s parameters from the inspiral wave form?” *Phys. Rev. D* **49**, 2658–2697 (1994), [arXiv:gr-qc/9402014](#).
- [17] J. Veitch *et al.*, “Parameter estimation for compact binaries with ground-based gravitational-wave observations using the LALInference software library,” *Phys. Rev. D* **91**, 042003 (2015), [arXiv:1409.7215 \[gr-qc\]](#).
- [18] Gregory Ashton *et al.*, “BILBY: A user-friendly Bayesian inference library for gravitational-wave astronomy,” *Astrophys. J. Suppl.* **241**, 27 (2019), [arXiv:1811.02042 \[astro-ph.IM\]](#).
- [19] Michael Boyle *et al.*, “The SXS Collaboration catalog of binary black hole simulations,” *Class. Quant. Grav.* **36**, 195006 (2019), [arXiv:1904.04831 \[gr-qc\]](#).
- [20] James Healy and Carlos O. Lousto, “Fourth RIT binary black hole simulations catalog: Extension to eccentric orbits,” *Phys. Rev. D* **105**, 124010 (2022), [arXiv:2202.00018 \[gr-qc\]](#).
- [21] Deborah Ferguson *et al.*, “Second MAYA Catalog of Binary Black Hole Numerical Relativity Waveforms,” (2023), [arXiv:2309.00262 \[gr-qc\]](#).
- [22] P. Ajith *et al.*, “Inspiral-merger-ringdown waveforms for black-hole binaries with non-precessing spins,” *Phys. Rev. Lett.* **106**, 241101 (2011), [arXiv:0909.2867 \[gr-qc\]](#).
- [23] L. Santamaria *et al.*, “Matching post-Newtonian and numerical relativity waveforms: systematic errors and a new phenomenological model for non-precessing black hole binaries,” *Phys. Rev. D* **82**, 064016 (2010), [arXiv:1005.3306 \[gr-qc\]](#).
- [24] Geraint Pratten, Sascha Husa, Cecilio Garcia-Quiros, Marta Colleoni, Antoni Ramos-Buades, Hector Estelles, and Rafel Jaume, “Setting the cornerstone for a family of models for gravitational waves from compact binaries: The dominant harmonic for nonprecessing quasi-circular black holes,” *Phys. Rev. D* **102**, 064001 (2020), [arXiv:2001.11412 \[gr-qc\]](#).
- [25] Cecilio García-Quiros, Marta Colleoni, Sascha Husa, Héctor Estellés, Geraint Pratten, Antoni Ramos-Buades, Maite Mateu-Lucena, and Rafel Jaume, “Multimode frequency-domain model for the gravitational wave signal from nonprecessing black-hole binaries,” *Phys. Rev. D* **102**, 064002 (2020), [arXiv:2001.10914 \[gr-qc\]](#).
- [26] Geraint Pratten *et al.*, “Computationally efficient models for the dominant and subdominant harmonic modes of precessing binary black holes,” *Phys. Rev. D* **103**, 104056 (2021), [arXiv:2004.06503 \[gr-qc\]](#).
- [27] A. Buonanno and T. Damour, “Effective one-body approach to general relativistic two-body dynamics,” *Phys. Rev. D* **59**, 084006 (1999), [arXiv:gr-qc/9811091](#).
- [28] Lorenzo Pompili *et al.*, “Laying the foundation of the effective-one-body waveform models SEOBNRv5: Improved accuracy and efficiency for spinning nonprecessing binary black holes,” *Phys. Rev. D* **108**, 124035 (2023), [arXiv:2303.18039 \[gr-qc\]](#).

- [29] Mohammed Khalil, Alessandra Buonanno, Hector Estelles, Deyan P. Mihaylov, Serguei Ossokine, Lorenzo Pompili, and Antoni Ramos-Buades, “Theoretical groundwork supporting the precessing-spin two-body dynamics of the effective-one-body waveform models SEOBNRv5,” *Phys. Rev. D* **108**, 124036 (2023), [arXiv:2303.18143 \[gr-qc\]](#).
- [30] Antoni Ramos-Buades, Alessandra Buonanno, Héctor Estellés, Mohammed Khalil, Deyan P. Mihaylov, Serguei Ossokine, Lorenzo Pompili, and Mahlet Shiferaw, “Next generation of accurate and efficient multipolar precessing-spin effective-one-body waveforms for binary black holes,” *Phys. Rev. D* **108**, 124037 (2023), [arXiv:2303.18046 \[gr-qc\]](#).
- [31] Alessandro Nagar, Piero Rettegno, Rossella Gamba, Simone Albanesi, Angelica Albertini, and Sebastiano Bernuzzi, “Analytic systematics in next generation of effective-one-body gravitational waveform models for future observations,” *Phys. Rev. D* **108**, 124018 (2023), [arXiv:2304.09662 \[gr-qc\]](#).
- [32] Rossella Gamba, Danilo Chiaramello, and Sayan Neogi, “Toward efficient effective-one-body models for generic, nonplanar orbits,” *Phys. Rev. D* **110**, 024031 (2024), [arXiv:2404.15408 \[gr-qc\]](#).
- [33] Marta Colleoni, Felipe A. Ramis Vidal, Cecilio García-Quirós, Sarp Akçay, and Sayantani Bera, “Fast frequency-domain gravitational waveforms for precessing binaries with a new twist,” (2024), [arXiv:2412.16721 \[gr-qc\]](#).
- [34] Manuela Campanelli, Carlos O. Lousto, Yosef Zlochower, and David Merritt, “Maximum gravitational recoil,” *Phys. Rev. Lett.* **98**, 231102 (2007), [arXiv:gr-qc/0702133](#).
- [35] Fabian Hofmann, Enrico Barausse, and Luciano Rezzolla, “The final spin from binary black holes in quasi-circular orbits,” *Astrophys. J. Lett.* **825**, L19 (2016), [arXiv:1605.01938 \[gr-qc\]](#).
- [36] Enrico Barausse, Viktoriya Morozova, and Luciano Rezzolla, “On the mass radiated by coalescing black-hole binaries,” *Astrophys. J.* **758**, 63 (2012), [Erratum: *Astrophys. J.* 786, 76 (2014)], [arXiv:1206.3803 \[gr-qc\]](#).
- [37] Xisco Jiménez-Forsteza, David Keitel, Sascha Husa, Mark Hannam, Sebastian Khan, and Michael Pürrer, “Hierarchical data-driven approach to fitting numerical relativity data for nonprecessing binary black holes with an application to final spin and radiated energy,” *Phys. Rev. D* **95**, 064024 (2017), [arXiv:1611.00332 \[gr-qc\]](#).
- [38] James Healy and Carlos O. Lousto, “Remnant of binary black-hole mergers: New simulations and peak luminosity studies,” *Phys. Rev. D* **95**, 024037 (2017), [arXiv:1610.09713 \[gr-qc\]](#).
- [39] James Healy, Carlos O. Lousto, and Yosef Zlochower, “Remnant mass, spin, and recoil from spin aligned black-hole binaries,” *Phys. Rev. D* **90**, 104004 (2014), [arXiv:1406.7295 \[gr-qc\]](#).
- [40] Jose A. Gonzalez, Ulrich Sperhake, Bernd Bruegmann, Mark Hannam, and Sascha Husa, “Total recoil: The Maximum kick from nonspinning black-hole binary inspiral,” *Phys. Rev. Lett.* **98**, 091101 (2007), [arXiv:gr-qc/0610154](#).
- [41] Manuela Campanelli, Carlos O. Lousto, Yosef Zlochower, and David Merritt, “Large merger recoils and spin flips from generic black-hole binaries,” *Astrophys. J. Lett.* **659**, L5–L8 (2007), [arXiv:gr-qc/0701164](#).
- [42] Carlos O. Lousto and Yosef Zlochower, “Further insight into gravitational recoil,” *Phys. Rev. D* **77**, 044028 (2008), [arXiv:0708.4048 \[gr-qc\]](#).
- [43] Carlos O. Lousto, Yosef Zlochower, Massimo Dotti, and Marta Volonteri, “Gravitational Recoil From Accretion-Aligned Black-Hole Binaries,” *Phys. Rev. D* **85**, 084015 (2012), [arXiv:1201.1923 \[gr-qc\]](#).
- [44] Carlos O. Lousto and Yosef Zlochower, “Nonlinear Gravitational Recoil from the Mergers of Precessing Black-Hole Binaries,” *Phys. Rev. D* **87**, 084027 (2013), [arXiv:1211.7099 \[gr-qc\]](#).
- [45] Davide Gerosa and Michael Kesden, “PRECESSION: Dynamics of spinning black-hole binaries with python,” *Phys. Rev. D* **93**, 124066 (2016), [arXiv:1605.01067 \[astro-ph.HE\]](#).
- [46] James Healy and Carlos O. Lousto, “Hangup effect in unequal mass binary black hole mergers and further studies of their gravitational radiation and remnant properties,” *Phys. Rev. D* **97**, 084002 (2018), [arXiv:1801.08162 \[gr-qc\]](#).
- [47] Frank Herrmann, Ian Hinder, Deirdre M. Shoemaker, Pablo Laguna, and Richard A. Matzner, “Binary Black Holes: Spin Dynamics and Gravitational Recoil,” *Phys. Rev. D* **76**, 084032 (2007), [arXiv:0706.2541 \[gr-qc\]](#).
- [48] Luciano Rezzolla, Enrico Barausse, Ernst Nils Dorband, Denis Pollney, Christian Reisswig, Jennifer Seiler, and Sascha Husa, “On the final spin from the coalescence of two black holes,” *Phys. Rev. D* **78**, 044002 (2008), [arXiv:0712.3541 \[gr-qc\]](#).
- [49] Luciano Rezzolla, Peter Diener, Ernst Nils Dorband, Denis Pollney, Christian Reisswig, Erik Schnetter, and Jennifer Seiler, “The Final spin from the coalescence of aligned-spin black-hole binaries,” *Astrophys. J. Lett.* **674**, L29–L32 (2008), [arXiv:0710.3345 \[gr-qc\]](#).
- [50] Michael Kesden, “Can binary mergers produce maximally spinning black holes?” *Phys. Rev. D* **78**, 084030 (2008), [arXiv:0807.3043 \[astro-ph\]](#).
- [51] Wolfgang Tichy and Pedro Marronetti, “The Final mass and spin of black hole mergers,” *Phys. Rev. D* **78**, 081501 (2008), [arXiv:0807.2985 \[gr-qc\]](#).
- [52] Enrico Barausse and Luciano Rezzolla, “Predicting the direction of the final spin from the coalescence of two black holes,” *Astrophys. J. Lett.* **704**, L40–L44 (2009), [arXiv:0904.2577 \[gr-qc\]](#).
- [53] Yosef Zlochower and Carlos O. Lousto, “Modeling the remnant mass, spin, and recoil from unequal-mass, precessing black-hole binaries: The Intermediate Mass Ratio Regime,” *Phys. Rev. D* **92**, 024022 (2015), [Erratum: *Phys. Rev. D* 94, 029901 (2016)], [arXiv:1503.07536 \[gr-qc\]](#).
- [54] Scott E. Field, Chad R. Galley, Jan S. Hesthaven, Jason Kaye, and Manuel Tiglio, “Fast prediction and evaluation of gravitational waveforms using surrogate models,” *Phys. Rev. X* **4**, 031006 (2014), [arXiv:1308.3565 \[gr-qc\]](#).
- [55] Jonathan Blackman, Scott E. Field, Chad R. Galley, Béla Szilágyi, Mark A. Scheel, Manuel Tiglio, and Daniel A. Hemberger, “Fast and Accurate Prediction of Numerical Relativity Waveforms from Binary Black Hole Coalescences Using Surrogate Models,” *Phys. Rev. Lett.* **115**, 121102 (2015), [arXiv:1502.07758 \[gr-qc\]](#).
- [56] Jonathan Blackman, Scott E. Field, Mark A. Scheel, Chad R. Galley, Daniel A. Hemberger, Patricia Schmidt, and Rory Smith, “A Surrogate Model of Gravitational Waveforms from Numerical Relativity Simula-

- tions of Precessing Binary Black Hole Mergers,” *Phys. Rev. D* **95**, 104023 (2017), [arXiv:1701.00550 \[gr-qc\]](#).
- [57] Vijay Varma, Scott E. Field, Mark A. Scheel, Jonathan Blackman, Lawrence E. Kidder, and Harald P. Pfeiffer, “Surrogate model of hybridized numerical relativity binary black hole waveforms,” *Phys. Rev. D* **99**, 064045 (2019), [arXiv:1812.07865 \[gr-qc\]](#).
- [58] Vijay Varma, Davide Gerosa, Leo C. Stein, François Hébert, and Hao Zhang, “High-accuracy mass, spin, and recoil predictions of generic black-hole merger remnants,” *Phys. Rev. Lett.* **122**, 011101 (2019), [arXiv:1809.09125 \[gr-qc\]](#).
- [59] Vijay Varma, Scott E. Field, Mark A. Scheel, Jonathan Blackman, Davide Gerosa, Leo C. Stein, Lawrence E. Kidder, and Harald P. Pfeiffer, “Surrogate models for precessing binary black hole simulations with unequal masses,” *Phys. Rev. Research* **1**, 033015 (2019), [arXiv:1905.09300 \[gr-qc\]](#).
- [60] Tousif Islam, Vijay Varma, Jackie Lodman, Scott E. Field, Gaurav Khanna, Mark A. Scheel, Harald P. Pfeiffer, Davide Gerosa, and Lawrence E. Kidder, “Eccentric binary black hole surrogate models for the gravitational waveform and remnant properties: comparable mass, nonspinning case,” *Phys. Rev. D* **103**, 064022 (2021), [arXiv:2101.11798 \[gr-qc\]](#).
- [61] Tousif Islam, Scott E. Field, Scott A. Hughes, Gaurav Khanna, Vijay Varma, Matthew Giesler, Mark A. Scheel, Lawrence E. Kidder, and Harald P. Pfeiffer, “Surrogate model for gravitational wave signals from nonspinning, comparable-to large-mass-ratio black hole binaries built on black hole perturbation theory waveforms calibrated to numerical relativity,” *Phys. Rev. D* **106**, 104025 (2022), [arXiv:2204.01972 \[gr-qc\]](#).
- [62] Jooheon Yoo, Vijay Varma, Matthew Giesler, Mark A. Scheel, Carl-Johan Haster, Harald P. Pfeiffer, Lawrence E. Kidder, and Michael Boyle, “Targeted large mass ratio numerical relativity surrogate waveform model for GW190814,” *Phys. Rev. D* **106**, 044001 (2022), [arXiv:2203.10109 \[gr-qc\]](#).
- [63] Jooheon Yoo *et al.*, “Numerical relativity surrogate model with memory effects and post-Newtonian hybridization,” *Phys. Rev. D* **108**, 064027 (2023), [arXiv:2306.03148 \[gr-qc\]](#).
- [64] Chad R. Galley and Patricia Schmidt, “Fast and efficient evaluation of gravitational waveforms via reduced-order spline interpolation,” (2016), [arXiv:1611.07529 \[gr-qc\]](#).
- [65] Michael Pürrer, “Frequency domain reduced order model of aligned-spin effective-one-body waveforms with generic mass-ratios and spins,” *Phys. Rev. D* **93**, 064041 (2016), [arXiv:1512.02248 \[gr-qc\]](#).
- [66] Yoshinta Setyawati, Michael Pürrer, and Frank Ohme, “Regression methods in waveform modeling: a comparative study,” *Class. Quant. Grav.* **37**, 075012 (2020), [arXiv:1909.10986 \[astro-ph.IM\]](#).
- [67] Sebastian Khan and Rhys Green, “Gravitational-wave surrogate models powered by artificial neural networks,” *Phys. Rev. D* **103**, 064015 (2021), [arXiv:2008.12932 \[gr-qc\]](#).
- [68] Stefano Schmidt, Matteo Breschi, Rossella Gamba, Giulia Pagano, Piero Rettengo, Gunnar Riemenschneider, Sebastiano Bernuzzi, Alessandro Nagar, and Walter Del Pozzo, “Machine Learning Gravitational Waves from Binary Black Hole Mergers,” *Phys. Rev. D* **103**, 043020 (2021), [arXiv:2011.01958 \[gr-qc\]](#).
- [69] Styliani-Christina Fragkouli, Paraskevi Nousi, Nikolaos Passalis, Panagiotis Iosif, Nikolaos Stergioulas, and Anastasios Tefas, “Deep Residual Error and Bag-of-Tricks Learning for Gravitational Wave Surrogate Modeling,” (2022), [arXiv:2203.08434 \[astro-ph.IM\]](#).
- [70] Lucy M. Thomas, Geraint Pratten, and Patricia Schmidt, “Accelerating multimodal gravitational waveforms from precessing compact binaries with artificial neural networks,” *Phys. Rev. D* **106**, 104029 (2022), [arXiv:2205.14066 \[gr-qc\]](#).
- [71] Ruijun Shi, Yue Zhou, Tianyu Zhao, Zhixiang Ren, and Zhoujian Cao, “Rapid eccentric spin-aligned binary black hole waveform generation based on deep learning,” (2024), [arXiv:2411.14893 \[gr-qc\]](#).
- [72] Victoria Tiki, Kiet Pham, and Eliu Huerta, “AI forecasting of higher-order wave modes of spinning binary black hole mergers,” (2024), [arXiv:2409.03833 \[gr-qc\]](#).
- [73] Osvaldo Gramaxo Freitas, Anastasios Theodoropoulos, Nino Villanueva, Tiago Fernandes, Solange Nunes, José A. Font, Antonio Onofre, Alejandro Torres-Forné, and José D. Martín-Guerrero, “NRSurNN3dq4: A Deep Learning Powered Numerical Relativity Surrogate for Binary Black Hole Waveforms,” (2024), [arXiv:2412.06946 \[gr-qc\]](#).
- [74] Zhiqiang Que *et al.*, “Accelerating Recurrent Neural Networks for Gravitational Wave Experiments,” in *32nd IEEE International Conference on Application-specific Systems, Architectures and Processors* (2021) [arXiv:2106.14089 \[cs.LG\]](#).
- [75] Alvin J. K. Chua, Chad R. Galley, and Michele Valisneri, “Reduced-order modeling with artificial neurons for gravitational-wave inference,” *Phys. Rev. Lett.* **122**, 211101 (2019), [arXiv:1811.05491 \[astro-ph.IM\]](#).
- [76] Jacopo Tissino, Gregorio Carullo, Matteo Breschi, Rossella Gamba, Stefano Schmidt, and Sebastiano Bernuzzi, “Combining effective-one-body accuracy and reduced-order-quadrature speed for binary neutron star merger parameter estimation with machine learning,” *Phys. Rev. D* **107**, 084037 (2023), [arXiv:2210.15684 \[gr-qc\]](#).
- [77] Dwyer S. Deighan, Scott E. Field, Collin D. Capano, and Gaurav Khanna, “Genetic-algorithm-optimized neural networks for gravitational wave classification,” (2020), [10.1007/s00521-021-06024-4](#), [arXiv:2010.04340 \[gr-qc\]](#).
- [78] C. V. Vishveshwara, “Stability of the schwarzschild metric,” *Phys. Rev. D* **1**, 2870–2879 (1970).
- [79] William H. Press, “Long Wave Trains of Gravitational Waves from a Vibrating Black Hole,” *Astrophys. J. Lett.* **170**, L105–L108 (1971).
- [80] Richard H. Price, “Nonspherical perturbations of relativistic gravitational collapse. i. scalar and gravitational perturbations,” *Phys. Rev. D* **5**, 2419–2438 (1972).
- [81] Richard H. Price, “Nonspherical perturbations of relativistic gravitational collapse. ii. integer-spin, zero-rest-mass fields,” *Phys. Rev. D* **5**, 2439–2454 (1972).
- [82] Emanuele Berti, Vitor Cardoso, and Andrei O. Starinets, “Quasinormal modes of black holes and black branes,” *Class. Quant. Grav.* **26**, 163001 (2009), [arXiv:0905.2975 \[gr-qc\]](#).
- [83] Saul A. Teukolsky, “The Kerr Metric,” *Class. Quant. Grav.* **32**, 124006 (2015), [arXiv:1410.2130 \[gr-qc\]](#).

- [84] David Merritt, Milos Milosavljevic, Marc Favata, Scott A. Hughes, and Daniel E. Holz, “Consequences of gravitational radiation recoil,” *Astrophys. J. Lett.* **607**, L9–L12 (2004), [arXiv:astro-ph/0402057](#).
- [85] J. A. Gonzalez, M. D. Hannam, U. Sperhake, Bernd Bruegmann, and S. Husa, “Supermassive recoil velocities for binary black-hole mergers with antialigned spins,” *Phys. Rev. Lett.* **98**, 231101 (2007), [arXiv:gr-qc/0702052](#).
- [86] Davide Gerosa and Alberto Sesana, “Missing black holes in brightest cluster galaxies as evidence for the occurrence of superkicks in nature,” *Mon. Not. Roy. Astron. Soc.* **446**, 38–55 (2015), [arXiv:1405.2072 \[astro-ph.GA\]](#).
- [87] Vijay Varma, Sylvia Biscoveanu, Tousif Islam, Feroz H. Shaik, Carl-Johan Haster, Maximiliano Isi, Will M. Farr, Scott E. Field, and Salvatore Vitale, “Evidence of Large Recoil Velocity from a Black Hole Merger Signal,” *Phys. Rev. Lett.* **128**, 191102 (2022), [arXiv:2201.01302 \[astro-ph.HE\]](#).
- [88] Vijay Varma, Maximiliano Isi, and Sylvia Biscoveanu, “Extracting the Gravitational Recoil from Black Hole Merger Signals,” *Phys. Rev. Lett.* **124**, 101104 (2020), [arXiv:2002.00296 \[gr-qc\]](#).
- [89] Lucy M. Thomas, “Gwbonsai: Building and optimising neural surrogates for astrophysical inference,” (2025).
- [90] Takuya Akiba, Shotaro Sano, Toshihiko Yanase, Takeru Ohta, and Masanori Koyama, “Optuna: A next-generation hyperparameter optimization framework,” in *Proceedings of the 25th ACM SIGKDD International Conference on Knowledge Discovery and Data Mining, KDD ’19* (Association for Computing Machinery, New York, NY, USA, 2019) p. 2623–2631.
- [91] James Bergstra, Daniel Yamins, and David Cox, “Making a science of model search: Hyperparameter optimization in hundreds of dimensions for vision architectures,” in *Proceedings of the 30th International Conference on Machine Learning*, Proceedings of Machine Learning Research, Vol. 28, edited by Sanjoy Dasgupta and David McAllester (PMLR, Atlanta, Georgia, USA, 2013) pp. 115–123.
- [92] Martín Abadi, Ashish Agarwal, Paul Barham, Eugene Brevdo, Zhifeng Chen, Craig Citro, Greg S. Corrado, Andy Davis, Jeffrey Dean, Matthieu Devin, Sanjay Ghemawat, Ian Goodfellow, Andrew Harp, Geoffrey Irving, Michael Isard, Yangqing Jia, Rafal Jozefowicz, Lukasz Kaiser, Manjunath Kudlur, Josh Levenberg, Dandelion Mané, Rajat Monga, Sherry Moore, Derek Murray, Chris Olah, Mike Schuster, Jonathon Shlens, Benoit Steiner, Ilya Sutskever, Kunal Talwar, Paul Tucker, Vincent Vanhoucke, Vijay Vasudevan, Fernanda Viégas, Oriol Vinyals, Pete Warden, Martin Wattenberg, Martin Wicke, Yuan Yu, and Xiaoqiang Zheng, “TensorFlow: Large-scale machine learning on heterogeneous systems,” (2015), software available from tensorflow.org.
- [93] Adam Paszke *et al.*, “PyTorch: An Imperative Style, High-Performance Deep Learning Library,” (2019), [arXiv:1912.01703 \[cs.LG\]](#).
- [94] Charles R. Harris, K. Jarrod Millman, Stéfan J. van der Walt, Ralf Gommers, Pauli Virtanen, David Cournapeau, Eric Wieser, Julian Taylor, Sebastian Berg, Nathaniel J. Smith, Robert Kern, Matti Picus, Stephan Hoyer, Marten H. van Kerkwijk, Matthew Brett, Allan Haldane, Jaime Fernández del Río, Mark Wiebe, Pearu Peterson, Pierre Gérard-Marchant, Kevin Sheppard, Tyler Reddy, Warren Weckesser, Hameer Abbasi, Christoph Gohlke, and Travis E. Oliphant, “Array programming with NumPy,” *Nature* **585**, 357–362 (2020).
- [95] James Bradbury, Roy Frostig, Peter Hawkins, Matthew James Johnson, Chris Leary, Dougal Maclaurin, George Necula, Adam Paszke, Jake VanderPlas, Skye Wanderman-Milne, and Qiao Zhang, “Jax: composable transformations of python+numpy programs,” (2018).
- [96] Fabian Pedregosa, Gaël Varoquaux, Alexandre Gramfort, Vincent Michel, Bertrand Thirion, Olivier Grisel, Mathieu Blondel, Peter Prettenhofer, Ron Weiss, Vincent Dubourg, Jake Vanderplas, Alexandre Passos, David Cournapeau, Matthieu Brucher, Matthieu Perrot, and Édouard Duchesnay, “Scikit-learn: Machine learning in python,” *Journal of Machine Learning Research* **12**, 2825–2830 (2011).
- [97] James Bergstra, Rémi Bardenet, Yoshua Bengio, and Balázs Kégl, “Algorithms for hyper-parameter optimization,” *Advances in Neural Information Processing Systems* **24** (2011).
- [98] Xavier Glorot and Yoshua Bengio, “Understanding the difficulty of training deep feedforward neural networks,” *Proceedings of the Thirteenth International Conference on Artificial Intelligence and Statistics* **9**, 249–256 (2010).
- [99] Vijay Varma, Leo C. Stein, Matteo Boschini, Scott E. Field, and Davide Gerosa, “surfinbh: Surrogate final bh properties,” (2018).
- [100] LIGO Scientific Collaboration, Virgo Collaboration, and KAGRA Collaboration, “Lvkm algorithm library - lalsuite,” Free software, GPL (2018).